IEEE Access
Multidisciplinary | Rapid Review | Open Access Journal

Received December 19, 2021, accepted January 9, 2022, date of publication January 31, 2022, date of current version February 11, 2022.

Digital Object Identifier 10.1109/ACCESS.2022.3147822

On the Development of Metal 3D Printed Bandpass Filter With Wide Stopband Based on Deformed Elliptical Cavity Resonator With an Additional Plate

POVILAS VAITUKAITIS[1], (Graduate Student Member, IEEE), KENNETH NAI[2], JIAYU RAO[1], (Graduate Student Member, IEEE), AND JIASHENG HONG[1], (Fellow, IEEE)

[1]School of Engineering and Physical Sciences, Heriot-Watt University, Edinburgh EH14 4AS, U.K.
[2]Renishaw Plc, Wotton-under-Edge, Gloucestershire GL12 8JR, U.K.

Corresponding author: Povilas Vaitukaitis (pv30@hw.ac.uk)

This work was supported in part by the Engineering and Physical Sciences Research Council (EPSRC), and in part by Renishaw Plc through the Industrial Cooperative Awards in Science and Technology (ICASE) Studentship (Voucher number 19000147 under Grant EP/T517471/1).

ABSTRACT This paper presents a newly developed metal 3D printed waveguide bandpass filter based on a modified deformed elliptical cavity resonator with an additional plate. The modified resonator has excellent design freedom allowing semi-independent control of centre frequency, bandwidth, and transmission zeros. Furthermore, transmission zeros can be placed close and far from the passband to improve frequency selectivity and stopband's width and rejection, respectively. Theory of the resonator, filter design with an example, and simulated and experimental results with extensive discussion are given. As proof of concept, a 5-pole *Ku*-band wideband filter was designed and manufactured using Selective Laser Melting, a metal 3D printing technique. Even though the prototypes were tested as-built, i.e. without any surface post-processing, the simulated and measured results have good agreement and consistency between all four printed prototypes. Moreover, the prototypes were manufactured in one piece, significantly improving measured results compared to the previous two-piece prototypes.

INDEX TERMS Deformed cavity resonator, metal 3D printing, selective laser melting, waveguide filter, wideband bandpass filter, wide stopband.

I. INTRODUCTION

Microwave resonators are a fundamental part of any wireless communication systems. Due to the development of new communication applications, which require higher data transfer rates and thus use higher frequency bands, and the ever-increasing number of users of those applications, the spectrum must be fully utilised [1]. This puts stringent requirements on microwave filters. Waveguide filters are commonly used at higher frequencies as they have desired properties such as low insertion loss, high selectivity, and high power handling. However, as a trade-off, waveguide filters generally have a large footprint. Therefore, developing new filter designs with improved performance and reduced footprint is essential to support the development of future communication applications.

The associate editor coordinating the review of this manuscript and approving it for publication was Xi Zhu.

Additive manufacturing (AM) or 3D printing offers various advantages: no tooling costs, reduced lead time, rapid prototyping, lightweight structures, and reduced material waste. However, perhaps the most significant advantage of AM is design and geometrical freedom, which allows improving performance and reducing the footprint of microwave components, and integrating different functions [2]–[5]. Metal 3D printing is a relatively new technique as only Laser Beam Powder Bed Fusion (LB-PBF) technologies have achieved widespread use in the industry [6]. This manufacturing technique is not without disadvantages as it has a rough surface finish and limited dimensional accuracy. However, if utilised to the fullest, design freedom can offer excellent performance despite these disadvantages [3], [7], [8]. Moreover, there are mitigating techniques to reduce the impact of rough surface finish and dimensional accuracy [9].

This paper presents a newly designed and monolithically 3D printed metal waveguide filter based on a deformed

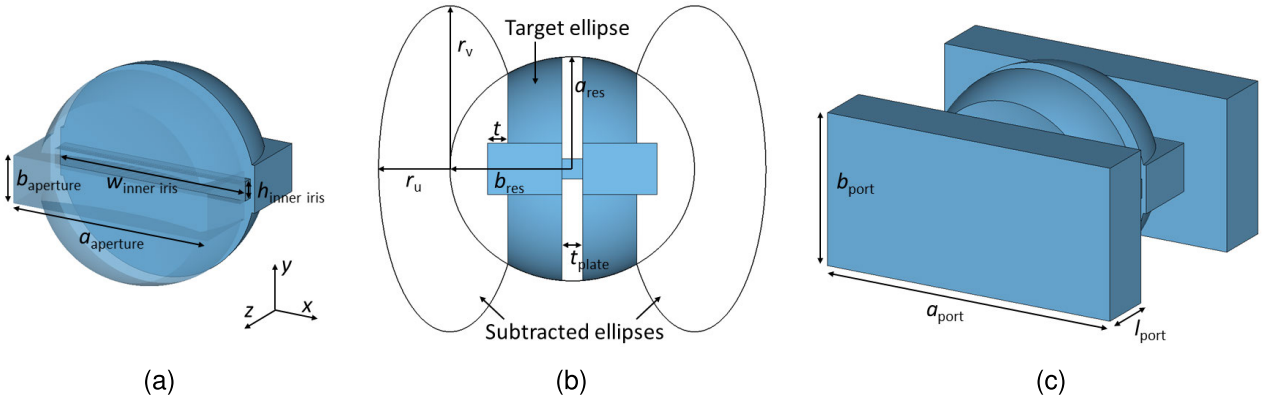

FIGURE 1. The inside volume of the deformed elliptical cavity resonator with an additional plate in the middle. (a) Perspective view with the transparent front half of the ellipsoid. (b) Side view. (c) Perspective view of the complete resonator with standard WG18 waveguide ports.

TABLE 1. Parameters of the base case.

Parameter	Value (mm)	Parameter	Value (mm)
$a_{aperture}$	11.5	$b_{aperture}$	2.5
$w_{inner\ iris}$	11.25	$h_{inner\ iris}$	1
a_{res}	5.75	b_{res}	6
r_v	8	r_u	3.5
t	1	t_{plate}	1
a_{port}	15.8	b_{port}	7.9
l_{port}	3		

Refer to Fig. 1 for parameter definitions.

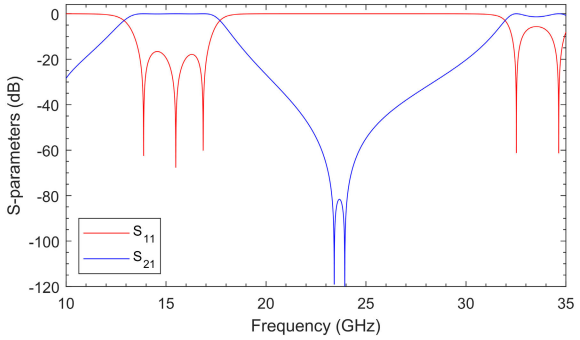

FIGURE 2. Frequency response of the base case.

elliptical cavity resonator with an additional plate, a modified version of the resonator from [10]. The additional plate serves three functions: splits one of the propagating modes into two, thus introducing extra pole and transmission zero (TZ); suppresses spurious resonances by forming narrow iris; and acts as a support for the overhanging top surface, which aids in manufacturing the model in one piece. Previously, a 5-pole filter prototype of this type was 3D printed in two pieces using Selective Laser Melting (SLM), and the preliminary results were reported at a conference [11]. Compared to the conference paper, this article extends the theory, adds filter design, adds one piece filter prototype experimental results, and expands the discussion of simulated and measured results.

The paper outline is as follows. Section II explains the construction of the resonator and working principle. Section III demonstrates how to design a filter based on the resonator. Section IV gives prototype filter's simulated and experimental results and further discussion, including sensitivity analysis and comparison with other works.

II. RESONATOR

A. RESONATOR STRUCTURE AND DIMENSIONS

The inside volume of the resonator with key dimensions is shown in Fig. 1. The resonator is constructed by subtracting two identical ellipsoids from the sides of the main ellipsoid, adding a rectangular aperture, subtracting the plate to form a narrow inner iris, and then adding standard waveguide ports. Note that all ellipsoids have the same dimensions in x and y directions. The first interesting thing about this resonator is that the waveguide ports are part of the resonator, contrary to the typical resonator. Without them, two of the three propagating modes would not be formed.

B. THEORY

The typical, base case resonator response is shown in Fig. 2, with all dimensions displayed in Table 1. This base case will be used throughout the paper for parametric studies. The three poles in the passband are the TE_{101} mode of the rectangular cavity, and quasi-TE_{102} and quasi-TE_{103} modes of the split elliptical cavity. The latter two modes are not formed without the waveguide ports. The H-fields of all three modes are shown in Fig. 3.

The second interesting thing about this resonator is that the first two spurious resonances typically are not excited at around 20.5 GHz from the TM_{110} modes of the split elliptical cavity. Hence, these resonances are not visible in Fig. 2. The rectangular apertures have to be moved up or down to break the symmetry of excitation of the spilt elliptical cavity in order to excite the TM_{110} modes. Therefore, the stopband

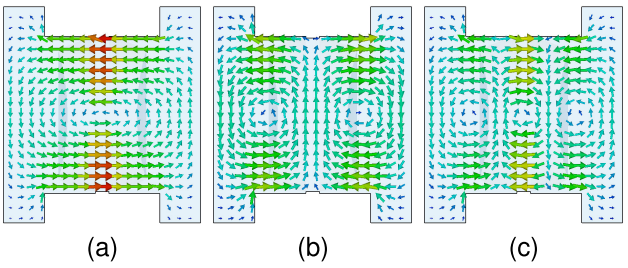

FIGURE 3. Base case cross-section view of the magnetic field of the: (a) TE_{101} mode at 14.11 GHz; (b) quasi-TE_{102} mode at 17.08 GHz; (c) quasi-TE_{103} mode at 18.19 GHz.

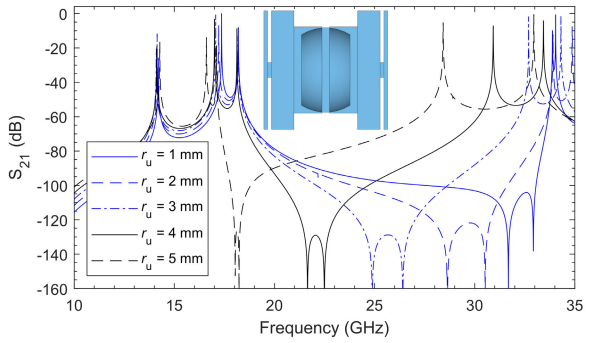

FIGURE 4. Weak I/O coupling S_{21} response for different r_u parameter values (inset: top view of 3D resonator model with weak I/O coupling).

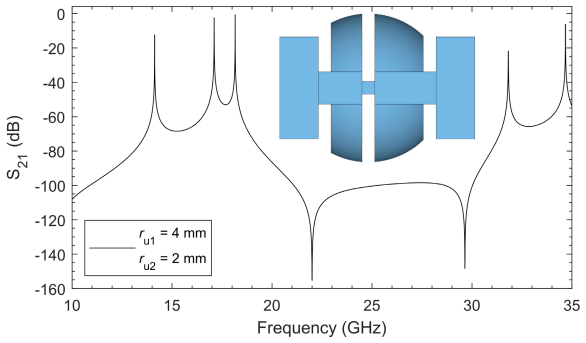

FIGURE 5. Weak I/O coupling S_{21} response of the base case with different r_{u1} and r_{u2} values. r_{u1} corresponds to the left side of the model and first TZ, and r_{u2} to the right and second TZ (inset: side view of 3D resonator model).

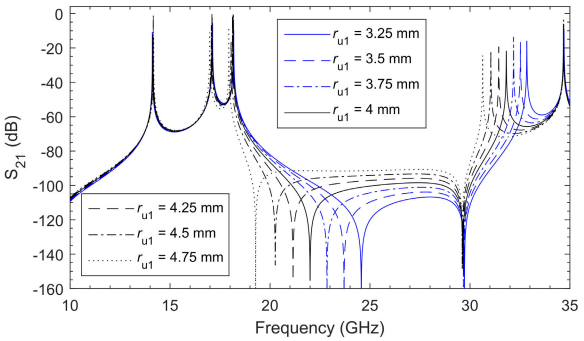

FIGURE 6. Weak I/O coupling S_{21} response for different r_{u1} values.

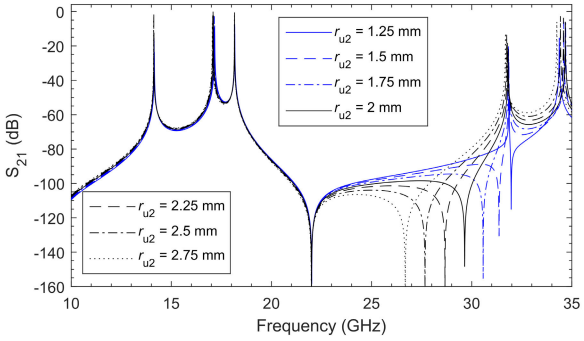

FIGURE 7. Weak I/O coupling S_{21} response for different r_{u2} values.

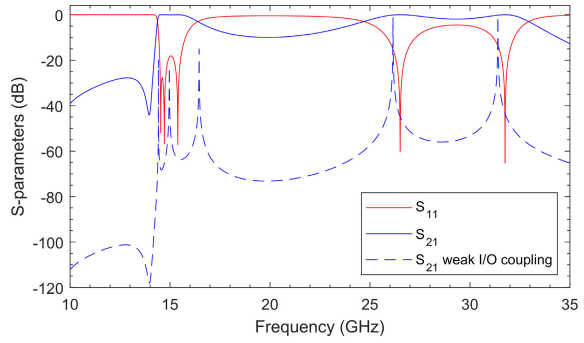

FIGURE 8. Frequency response of the resonator with both TZs below the passband.

is increased significantly without any effort. In addition, TM_{110} modes might prove useful in designing dual-band filters, as discussed later.

C. TRANSMISSION ZEROS

The pair of TZs is mainly controlled via the r_u parameter, as shown in Fig. 4. Notice how TZs are squeezing the modes when r_u is equal to 1 mm or 5 mm. That indicates how TZs can suppress mode resonances. However, as passband modes can also be suppressed, TZs cannot be moved too close to the passband. Hence, transmission zeros cannot significantly improve selectivity and are instead used to obtain a wide stopband with high rejection.

Furthermore, each TZ can be controlled individually by changing subtracted ellipsoids, c.f. Fig. 1b, to be non-identical. The base case for this example is shown in Fig. 5 with the side view of the corresponding 3D model. Figs. 6 and 7 illustrate how to control the first TZ and second TZ using r_{u1} and r_{u2}, respectively. In both cases, only one TZ moves while the frequency of the another TZ and all the modes remains essentially unaffected.

At this point, it might seem like both TZs are formed and controlled by the second passband's modes, especially looking at Fig. 6. However, this is not the case, as it is possible to move TZs below the passband by shifting TE_{101} mode above both quasi modes, i.e., by changing the sign of the coupling coefficient, as shown in Fig. 8. Several parameters

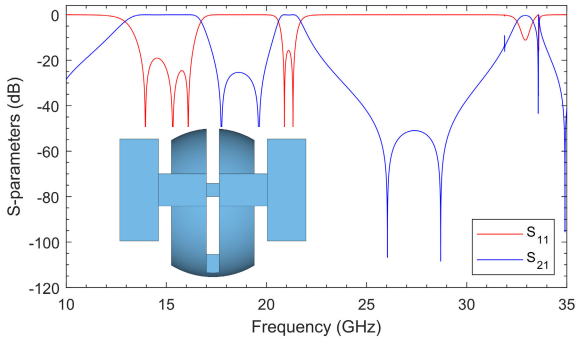

FIGURE 9. Frequency response of the dual-band resonator (inset: side view of 3D resonator model).

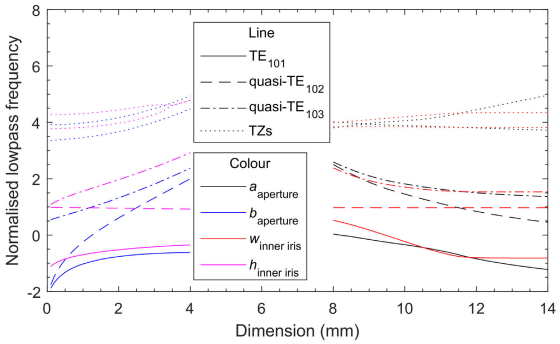

FIGURE 10. Normalised lowpass frequency of all three modes propagating in the passband and two transmission zeros for a_{aperture}, b_{aperture}, $w_{\text{inner iris}}$, and $h_{\text{inner iris}}$.

had to be changed to swap the modes: $a_{\text{aperture}} = 9.5$ mm, $a_{\text{res}} = 6.75$ mm, $r_{\text{u}} = 5.2$ mm, and $w_{\text{inner iris}} = 9.5$ mm. Enlarging the elliptical cavity and decreasing the width of the rectangular aperture puts quasi-TE_{102} at 14.42 GHz, quasi-TE_{103} at 14.965 GHz, and TE_{101} at 16.45 GHz. It should be noted that the TE_{101} mode's H-field remains unchanged, but both quasi modes have quite different H-fields.

D. DUAL-BAND RESONATOR

Fig. 9 shows the frequency response when TM_{110} modes of the split elliptical cavity are excited, resulting in a potential of dual-band response. The dual-band response is achieved by either moving rectangular apertures and the inner iris or the elliptical cavity lower or higher to disturb the symmetry of excitation of the TM_{110} modes. The inset of Fig. 9 shows a side view of the resonator where the elliptical cavity was moved lower by 1 mm. Note that a small aperture of 3.75 mm × 1.75 mm is added between the split elliptical cavities to improve TM_{110} modes' coupling. All other dimensions are the same as in Table 1.

The response shown in Fig. 9 is dual-band, with the first passband being wider and having one extra pole due to the TE_{101} mode than the second passband. There are two TZs between the bands to increase the rejection and two more TZs above the second passband. However, quasi modes and TM modes are mainly controlled by the split elliptical cavity parameters. Therefore, it might be hard or impossible to control centre frequencies, bandwidths, and TZs positions entirely independently. More degrees of freedom might help to improve independent control. For example, different parameters of the main elliptical cavity in x and y directions (c.f. Fig. 1), non-identical subtracted ellipsoids from the sides, or even non-identical split elliptical cavity halves. In addition, coupling between these various modes might be hard to realise and control, thus additional coupling structures might be needed. All of this remains to be explored in the future.

III. FILTER DESIGN

A. PARAMETRIC STUDY

The third interesting thing about the resonator is that when combining two or more resonators, TE_{101} modes of the rectangular apertures merge, hence contributing one pole per filter. Therefore, it is quite challenging or even impossible to work out sensible and physically accurate filter topology and corresponding coupling matrix representing physical filter. Even though the filter topology may be unobtainable, few things are certain. The filter order, N, is always an odd number because it is equal to $2 \times n + 1$, where n is the number of split elliptical cavities. The maximum number of TZs the filter can have is $N - 1$, corresponding to the number of split elliptical cavities. Additionally, higher order filters should be possible to realise as was shown with an 8-pole filter based on the previous resonator model in [10]. Although the optimisation part of the design is bound to be more complex and time consuming compared to the example given in this section.

Another way to demonstrate filter design is by performing a parametric study to understand how each parameter affects the frequency of the modes and pair of transmission zeros. The obtained parametric curves are then used to get initial guess for optimisation which yields the final filter parameters. Normalised lowpass frequency, f_{n}, (1) is used for easier and more accurate comparison:

$$f_n = \frac{1}{FBW}\left(\frac{f}{f_0} - \frac{f_0}{f}\right), \tag{1}$$

where f is the frequency, f_0 is the centre frequency, and FBW is the fractional bandwidth. The base case response in Fig. 2 is used to normalise the frequency, with $f_0 = 15.25$ GHz and $FBW = 22.61\%$. Refer to Fig. 1 for parameter definitions.

Fig. 10 displays normalised lowpass frequency of all propagating modes and pair of TZs for a_{aperture}, b_{aperture}, $w_{\text{inner iris}}$, and $h_{\text{inner iris}}$. a_{aperture} affects all three modes. $w_{\text{inner iris}}$ has a similar effect on TE_{101} and quasi-TE_{103} while not affecting quasi-TE_{102}. b_{aperture} and $h_{\text{inner iris}}$ have more control over all three modes. Notice how quasi modes converge to the same frequency as $h_{\text{inner iris}}$ approaches zero. This confirms that both quasi modes are split from one mode, as noted before. b_{aperture} and $h_{\text{inner iris}}$ are the two parameters that can bring all three modes near each other, thus controlling the bandwidth (BW). While the centre frequency decreases as

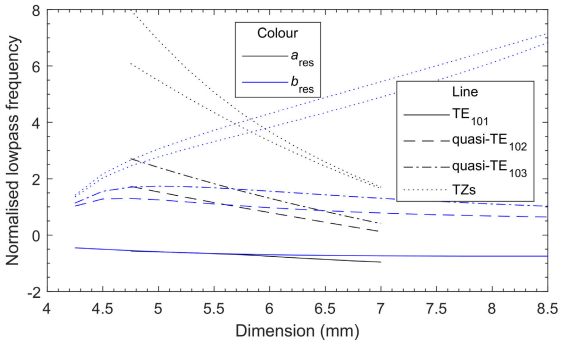

FIGURE 11. Normalised lowpass frequency of all three modes propagating in the passband and two transmission zeros for a_{res} and b_{res}.

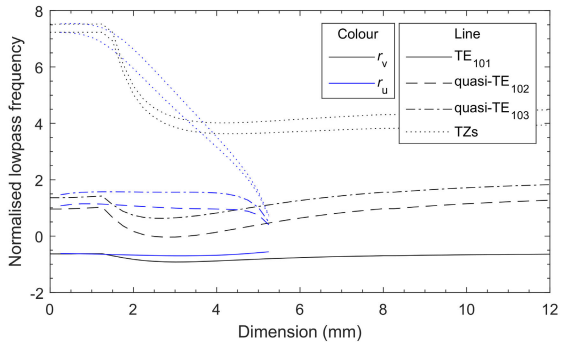

FIGURE 12. Normalised lowpass frequency of all three modes propagating in the passband and two transmission zeros for r_v and r_u.

these parameters decrease, it can be increased with a_{aperture} while maintaining similar separation between the modes. However, if printing in one piece, the dimensional accuracy and gap limit of SLM, puts restrictions on realisable BW. The smallest gap size to print without any reduction in quality is around 0.3-0.5 mm. Thus lowest FBW possible should be about 5-10%. None of these four parameters heavily affect the pair of TZs.

Figs. 11 and 12 show normalised lowpass frequency of all propagating modes and pair of TZs for a_{res} and b_{res}, and r_{v} and r_{u}, respectively. a_{res} is the main parameter to control quasi modes, as it affects them more than TE_{101}. However, it also heavily affects TZs. b_{res} or r_{u} can be used to correct that. Both can control TZs in almost the same manner with little effect on the frequency of the modes. Notice how whenever the thickness of the split elliptical cavity decreases, c.f. Fig. 1b, either r_{u} approaches b_{res} or vice versa, the pair of TZs starts squeezing the quasi modes. As mentioned earlier, this limits how close TZs can be placed to the passband. r_{v} only affects modes and TZs frequencies when smaller; as it increases, the effect decreases. However, r_{v} cannot be set too small because it will create an overhanging surface, c.f. Fig. 1b, which cannot be 3D printed or would reduce the manufacturing quality.

Fig. 13 shows normalised lowpass frequency of all propagating modes and pair of TZs for t_{plate}, t, and l_{port}. t_{plate} and t have some effect on quasi modes while almost none on

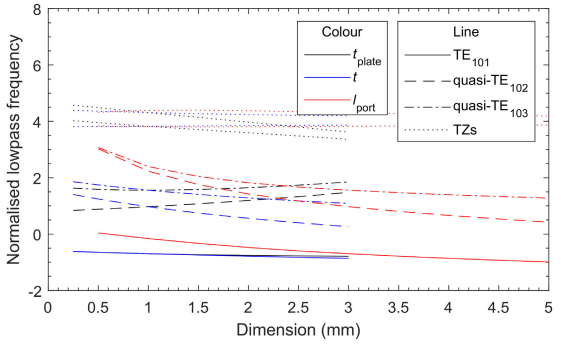

FIGURE 13. Normalised lowpass frequency of all three modes propagating in the passband and two transmission zeros for t_{plate}, t, and l_{port}.

TE_{101}; hence can be used as additional control parameters. l_{port} increases the frequency of all modes at shorter lengths; therefore, it cannot be set too small. There are also some other restrictions imposed by the manufacturing method. For example, t and t_{plate} cannot be set below 0.5-0.6 mm because thin walls are prone to warping due to thermal stresses [12].

To summarise: a_{aperture}, b_{aperture}, $w_{\text{inner iris}}$, $h_{\text{inner iris}}$, and a_{res} control centre frequency; b_{aperture} and $h_{\text{inner iris}}$ control bandwidth; and a_{res}, b_{res}, and r_{u} control transmission zeros. The remaining parameters, namely, r_{v}, t_{plate}, t, and l_{port}, are not that influential thus are used for fine-tuning.

B. OPTIMISATION

The filter design exploiting the novel deformed cavity and metal 3D printing capability is unique. It is an empirical method based on scaling the base case to the desired centre frequency and then using the parametric curves to manually vary several parameters to place TZs and simultaneously adjust bandwidth and centre frequency. After obtaining a reasonable initial guess, optimisation is used to achieve final filter specifications and parameter values. Full-wave simulation software CST Microwave Studio Suite [13] with Covariance Matrix Adaptation Evolutionary Strategy (CMA-ES) optimisation algorithm was used to optimise the filter. CMA-ES is a global optimiser well suited for complex problems with many variables such as this one.

A sample filter will be optimised to illustrate the filter design process. The simulations were run on a PC desktop with Intel(R) Core(TM) i7-4770 3.40 GHz CPU and 16 GB DDR3 RAM. The average time required to run a single simulation was approximately 44s. The filter has the same specifications as the manufactured prototype filter: $\text{N} = 5$, $\text{f}_1 = 13.75$ GHz, $\text{f}_2 = 16.5$ GHz, $\text{RL} = 20$ dB, and a wide stopband.

First, using the base case parameters scale to the desired centre frequency; in this case, no scaling was needed. Then position TZs and adjust bandwidth to obtain the initial guess for the optimisation. The first pair of TZs is placed close to the passband. From Fig. 12, it can be seen that the closest TZs can be set to the passband without affecting the modes is about $f_{\text{n}} = 2.5$, which is around 19 GHz for this filter. The second

TABLE 2. Parameters of the 5-pole filter optimisation example.

Parameter	Value (mm)			Parameter	Value (mm)			Parameter	Value (mm)		
	Initial	1st round	2nd round		Initial	1st round	2nd round		Initial	1st round	2nd round
$a_{\text{aperture1}}$	11.5	11.2766	11.2933	$a_{\text{aperture2}}$	11.5	11.5397	11.2485	$a_{\text{aperture3}}$	11.5	11.8317	11.6015
$b_{\text{aperture1}}$	2.5	2.9430	3.1041	$b_{\text{aperture2}}$	2.5	2	1.7489	$b_{\text{aperture3}}$	2.5	2.4168	2.0324
$w_{\text{inner iris1}}$	11.25	10.9674	11.0537	$w_{\text{inner iris2}}$	11.25	11.0020	11.1784	$h_{\text{inner iris1}}$	1	1.0609	1.0818
$h_{\text{inner iris2}}$	1	0.9212	0.8855	a_{res1}	6.5	6.2920	6.3906	a_{res2}	5.75	5.7736	5.7265
b_{res1}	6	5.3761	5.2500	b_{res2}	6	6.0186	5.9441	r_{v1}	8	8.1608	8.1063
r_{v2}	8	8.4664	8.4706	r_{u1}	3.75	3.8603	3.5351	r_{u2}	2	2.0154	1.9099
t_1	1	1.0587	1.1368	t_2	1	1.1249	1.1507	t_3	1	1.0943	1.1405
t_{plate1}	1	0.9846	0.9053	t_{plate2}	1	0.9703	0.9500	l_{port1}	3	3.2630	3.5218
l_{port2}	3	2.6052	2.6599								

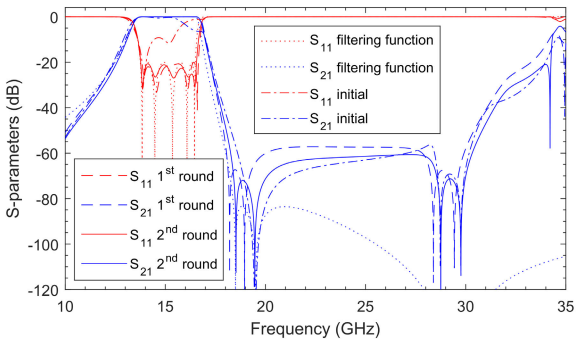

FIGURE 14. Filtering function, initial guess, and 1st and 2nd round of optimisation frequency response of 5-pole sample filter.

pair of TZs is placed far from the passband such that the stopband would have constant rejection and be as wide as possible. In this case the second pair of TZs is placed around 29 GHz. The initial guess parameters and response for this example are shown in Table 2 and Fig. 14, respectively.

Next, optimisation goals and parameter intervals must be set. The filtering function of the sample filter, shown in Fig. 14, can be used to obtain optimisation goals around the passband. Optimisation goals in the stopband can be defined after obtaining the initial guess response. All parameters' intervals were set to ±20% of the initial value. The first round took 1705 runs, about 19 hours. It was stopped before convergence because one of the parameters, $b_{\text{aperture2}}$, reached the lower boundary. Even then, the response after the first round was close to optimal, as seen in Fig. 14. For the second round, all parameters were set to ±20% of the first round value. Except for $b_{\text{aperture2}}$, for which the lower boundary was set to −50%. The second round took 2209 runs, 26.4 hours, to converge.

As seen in Fig. 14, the final response is slightly better than after the first round in terms of selectivity and stopband. The upper passband edge is not exactly the same compared to the filtering function, but it is at the acceptable level for this example. If required, further optimisation could be performed with revised optimisation goals. The

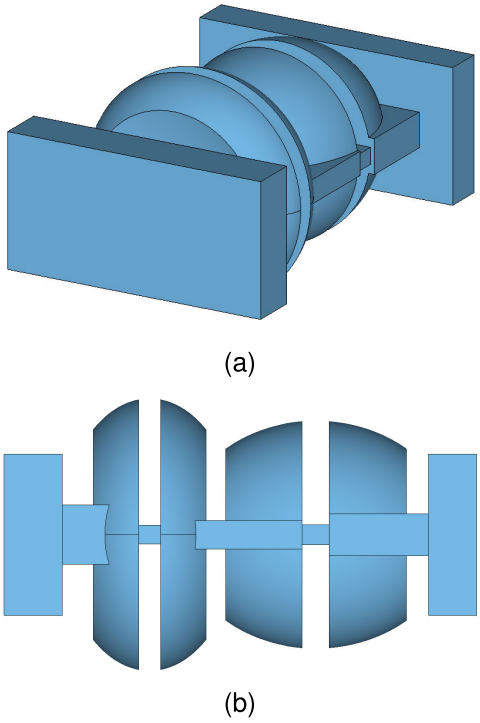

FIGURE 15. 5-pole prototype filter inside volume. (a) Perspective view. (b) Side view.

single TZ at 34.21 GHz is from the higher-order modes coupling. As shown in Table 2, all parameters, except $b_{\text{aperture1}}$, $b_{\text{aperture2}}$, and $b_{\text{aperture3}}$, remained well within ±20% of the initial value. Thus, the optimisation could have been done in a single round if a wider interval, e.g. ±50%, was applied to those three parameters.

IV. PROTOTYPE FILTER

A. SIMULATED RESULTS

The prototype filter is a 5-pole, centred at 15.06 GHz with 18.26% FBW. The 3D model and S-parameters are shown in Figs. 15 and 16, respectively. The 5-pole filter has improved

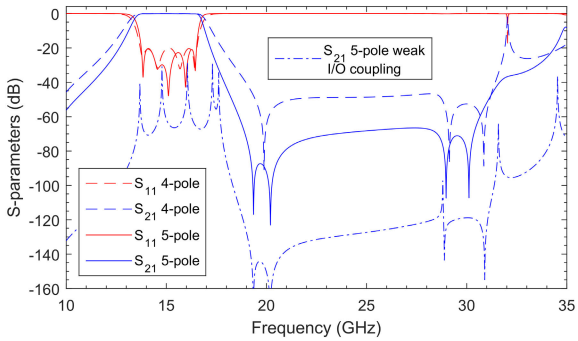

FIGURE 16. Frequency response of 4-pole and 5-pole prototype filters.

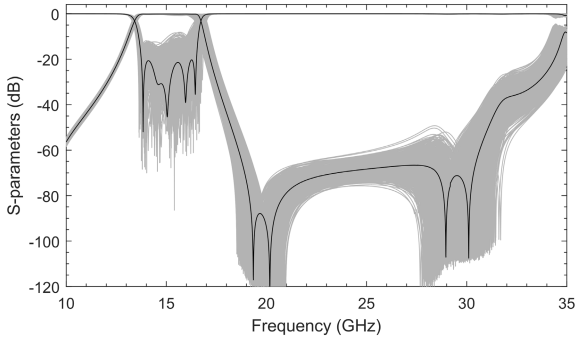

FIGURE 17. Sensitivity analysis of the 5-pole prototype filter with ±0.1 mm manufacturing dimensional accuracy.

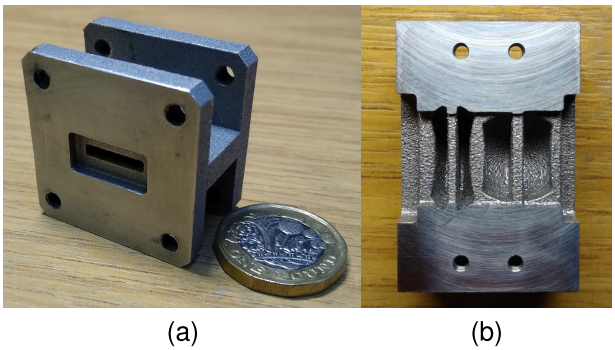

FIGURE 18. Metal 3D printed 5-pole prototype. (a) One piece perspective view with £1 coin for scale. (b) Two piece cross-section view.

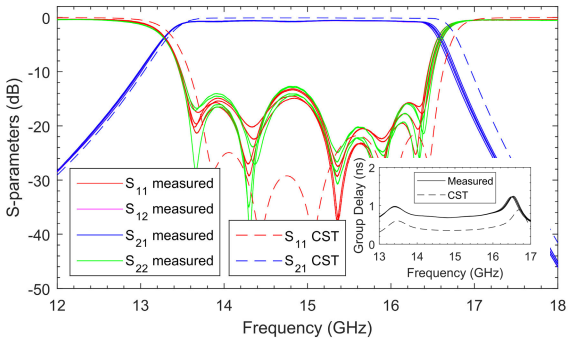

FIGURE 19. Inband frequency response of four 5-pole prototype filters (inset: group delay).

performance compared to the previous 4-pole filter [10] whilst maintaining an almost exact footprint of 33.30 mm × 33.30 mm × 23.12 mm (only 0.17 mm longer). It should be noted that this filter and the filter in the optimisation example are not precisely the same but have similar dimensions.

The eigenmode-simulated unloaded quality factor (Q_u) of a single resonator for the TE_{101}, quasi-TE_{102}, and quasi-TE_{103} modes is 2026, 2842, and 2558, respectively. The electrical conductivity $\sigma = 3.56 \times 10^7$ S/m for aluminium was used in the simulation. The previous resonator model had Q_u values of 2815 and 2842 for the TE_{101} and quasi-TE_{102} modes, respectively. A slight degradation of the Q_u is observed due to the additional mode.

The weak I/O coupling S_{21} response in Fig. 16 shows how spurious resonances are suppressed by TZ and narrow inner iris, at 28.8 GHz and 31.58 GHz, respectively. Together with TZs produced by higher-order modes coupling, c.f. Fig. 14, higher order filters could potentially suppress all second passband resonances between 28-36 GHz, thus increasing the stopband up to 40-45 GHz. This remains to be explored in the future.

B. SENSITIVITY ANALYSIS

A sensitivity analysis was performed to examine the fabrication tolerance effect of the SLM on the prototype filter. The analysis is based on the Monte Carlo sampling (MCS) method [14]. For a more realistic sensitivity analysis, all 29 parameters of the filter were included. The dimensional tolerance of the SLM is ±0.1 mm. However, it should be noted that this is the worst-case scenario, and the tolerance can be reduced by selecting the most appropriate build angle and other 3D printer settings.

Total 1000 simulation runs with uniformly random dimensions were performed to obtain the sensitivity analysis. The result is shown in Fig. 17. The filter is rather sensitive to the dimensional tolerance of ±0.1 mm. RL is mostly better than 10 dB, and there is a larger frequency variation at the upper edge of the passband. However, the wide stopband of the filter is maintained with similar rejection. Additionally, tuning screws could be added from both sides, or potentially top and bottom as well, of the filter for post-tuning which could improve inband response.

C. EXPERIMENTAL RESULTS AND DISCUSSION

The 5-pole prototype filter, shown in Fig. 18, was printed using SLM with RenAM 500Q AM system [23]. The material used was aluminium alloy powder, AlSi10Mg, which has appropriate electrical and mechanical properties [24], [25]. Four prototypes were printed monolithically at a 45° angle as it offers the best surface finish for all inner surfaces. The inband and wideband results are shown in Figs. 19 and 20, respectively. As observed, the agreement between measured and simulated results is adequate. The measured IL at the centre frequency is about 0.65 dB, and the RL across the passband is lower than 12.7 dB. It should be noted that the test fixture included two waveguide to coaxial adapters, which were not de-embedded and that the inner surface was not

TABLE 3. Comparison with previously reported bandpass filters.

Ref.	f_0 (GHz)	FBW (%)	N	IL (dB)	RL (dB)	Δf (%)	Q_u	Spurious suppression	f_{sp}/f_0	Manufacturing technology	Envelope (mm × mm × mm)
[4]	10	5	5	0.20-0.30	>15	0.90	3840-5195	Yes (>34 dB)	>1.80	SLM + surface polishing	41.40 × 41.40 × 94.00*
[15]	32.2	13.6	5	0.23-0.50	>17	0.37	N/A	—	N/A	SLA + EP Cu/ELP Ag	19.05 × 19.05 × 60.00
[16]	10	5	5	0.06-0.18	>20	0.05	14450	—	1.32	SLA + Cu plating	51.00 × 55.00 × 120.00*
[17]	11	12.82	8	N/A	>19*	N/A	N/A	Yes (>55 dB)	1.77	Milling + spark erosion	N/A
[18]	14.125	1.77	5	0.20	>18	<0.20	N/A	Yes (>55 dB)	>1.70	SLM + Ag plating	N/A
[19]	14.25	3.5	8	0.39-0.43	>22	N/A	>4500*	Yes (>55 dB)	>2.31	N/A	48.50 × 50.60 × 103.60
[20]	14.69	40.82	4*	0.43-0.60	>15	N/A	1080-1350	Yes (>70 dB)	>3.40	N/A	24.00 × 42.00 × 22.20
[21]	87.5	11.5	5	0.30-0.50	>18	2.78	N/A	—	N/A	SLA + EP Cu/Au	19.05 × 19.05 × 25.00*
[22]	32.17	5	4	0.43-1.00	>12	0.47	4644	—	1.37	SLA + ELP Cu/Ag	19.05 × 19.05 × 36.00
T.W.	15.06	18.26	5	0.52-0.83	>12.7	<1.07	2026-2842	Yes (>40 dB)	2.21	SLM as built	33.30 × 33.30 × 23.12

T.W. – this work; f_0 – centre frequency; FBW – fractional bandwidth; N – filter order; IL – insertion loss; RL – return loss; Δf – centre frequency shift; Q_u – simulated unloaded quality factor of a single resonator; f_{sp}/f_0 – first spurious resonance to centre frequency ratio; * – estimated value from figures and/or partial data from tables/text or other published papers by the same authors; N/A – not available; SLA – stereolithography; SLM – selective laser melting; EP – electroplating; ELP – electroless plating.

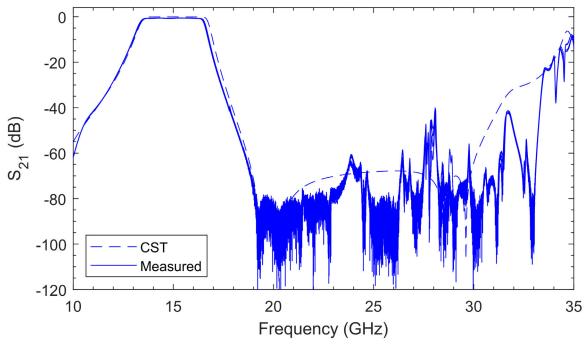

FIGURE 20. Wideband frequency response of four 5-pole prototype filters.

post-processed in any way. There is a larger frequency shift at the upper edge of the passband, as was predicted by the sensitivity analysis. The filter maintained a wide stopband with 40 dB rejection up to 33.3 GHz, about 2.21 times the centre frequency. The group delay is given in the inset of Fig. 19. The shift in group delay is caused mainly by the narrower bandpass of the measured filter and some extra delay from two waveguide to coaxial adapters.

The results are vastly better than the two-piece prototype [11]. Printing in one piece eliminated any assembly errors and potentially improved surface current flow as H-plane cut disturbed surface current of all propagating modes. Furthermore, the consistency of the results suggests that the dimensional inaccuracies or errors are similar, thus giving insight into reducing or eliminating them during the manufacturing process using optimisation methods [9].

Table 3 summarises a quantitative comparison of the prototype filter versus other reported bandpass filters. The prototype filter has the widest stopband compared to those filters manufactured using 3D printing. In addition, it has advantages of relatively easy design and manufacturing, compact footprint, and high power handling. Furthermore, IL and potentially RL could be improved with post-processing such as bead blasting, electro-polishing, or silver plating, and de-embedding the test fixture. This remains to be investigated in the future.

V. CONCLUSION

This paper presented a comprehensive study of a novel deformed elliptical cavity resonator with an additional plate to develop compact, high performance microwave filters exploiting advanced additive manufacturing technology. For demonstration, a 5-pole filter prototype was designed and monolithically manufactured using Selective Laser Melting. The measured results had a good agreement with the simulation and were an improvement over the previous prototype printed in two pieces. Furthermore, the filter is comparable with reported state-of-the-art bandpass filters. Several potential future R&D directions were identified in the paper, which include the design of a dual-band filter based on the same resonator.

ACKNOWLEDGMENT

The authors would like to thank the staff at Renishaw and James from the mechanical workshop at Heriot-Watt for their help in this project.

REFERENCES

[1] G. Maral, M. Bousquet, and Z. Sun, *Satellite Communications Systems: Systems, Techniques and Technology*, 6th ed. Hoboken, NJ, USA: Wiley, 2020, pp. 21–27.

[2] R. Sorrentino and O. A. Peverini, "Additive manufacturing: A key enabling technology for next-generation microwave and millimeter-wave systems [point of view]," *Proc. IEEE*, vol. 104, no. 7, pp. 1362–1366, Jul. 2016.
[3] C. Tomassoni, O. A. Peverini, G. Venanzoni, G. Addamo, F. Paonessa, and G. Virone, "3D printing of microwave and millimeter-wave filters: Additive manufacturing technologies applied in the development of high-performance filters with novel topologies," *IEEE Microw. Mag.*, vol. 21, no. 6, pp. 24–45, Jun. 2020.
[4] C. Guo, Y. Yu, S. Li, X. Wen, A. Zhang, Y. Wang, and M. Attallah, "Monolithic 3D printed waveguide filters with wide spurious-free stopbands using dimpled spherical resonators," *IET Microw., Antennas Propag.*, vol. 15, no. 12, pp. 1657–1670, Oct. 2021.
[5] X. Wen, C. Guo, X. Shang, Y. Yu, M. Shu, Q. Yang, S. Li, M. M. Attallah, H. Liu, and A. Zhang, "SLM printed waveguide dual-mode filters with reduced sensitivity to fabrication imperfections," *IEEE Microw. Wireless Compon. Lett.*, vol. 31, no. 11, pp. 1195–1198, Nov. 2021.
[6] M. Munsch, M. Schmidt-Lehr, and E. Wycisk, "Additive manufacturing: New metal technologies," AMPOWER GmbH & Co. KG, Hamburg, Germany, White Paper, 2020. [Online]. Available: https://ampower.eu/insights/new-metal-technologies/
[7] J. Rao, K. Nai, P. Vaitukaitis, Y. Li, and J. Hong, "3-D metal printed compact high-Q folded waveguide filter with folded antenna," *IEEE Trans. Microw. Theory Techn.*, vol. 70, no. 1, pp. 112–121, Jan. 2022.
[8] J. Rao, K. Nai, P. Vaitukaitis, Y. Li, and J. Hong, "Compact 3D metal printed filtering antenna," *IEEE Antennas Wireless Propag. Lett.*, early access, Dec. 2, 2021, doi: 10.1109/LAWP.2021.3132196.
[9] L. Cao, J. Li, J. Hu, H. Liu, Y. Wu, and Q. Zhou, "Optimization of surface roughness and dimensional accuracy in LPBF additive manufacturing," *Opt. Laser Technol.*, vol. 142, Oct. 2021, Art. no. 107246.
[10] P. Vaitukaitis, K. Nai, J. Rao, and J. Hong, "3D metal printed deformed elliptical cavity bandpass filter with wide stopband," to be presented at EuMC, Apr. 2–7, 2022.
[11] P. Vaitukaitis, K. Nai, J. Rao, and J. Hong, "3D metal printed deformed elliptical cavity bandpass filter with an additional plate," presented at the IEEE CPMT Symp. Jpn. (ICSJ), Kyoto, Japan, Nov. 2021.
[12] X. Lu, M. Chiumenti, M. Cervera, H. Tan, X. Lin, and S. Wang, "Warpage analysis and control of thin-walled structures manufactured by laser powder bed fusion," *Metals*, vol. 11, no. 5, p. 686, Apr. 2021.
[13] CST Studio Suite. (2019). *Dassault Systemes*. [Online]. Available: https://www.3ds.com/products-services/simulia/products/cst-studio-suite/
[14] J. Bornemann, U. Rosenberg, S. Amari, and R. Vahldieck, "Tolerance analysis of bypass-, cross-and direct-coupled rectangular waveguide band-pass filters," *IEE Proc. Microw. Antennas Propag.*, vol. 152, no. 3, pp. 167–170, 2005.
[15] J. Li, C. Guo, J. Xu, and L. Mao, "Lightweight low-cost Ka-band 3-D printed slotted rectangular waveguide bandpass filters," in *Proc. IEEE Int. Symp. Antennas Propag., USNC/URSI Nat. Radio Sci. Meeting*, Jul. 2017, pp. 2647–2648.
[16] C. Guo, X. Shang, M. J. Lancaster, and J. Xu, "A 3-D printed lightweight X-band waveguide filter based on spherical resonators," *IEEE Microw. Wireless Compon. Lett.*, vol. 25, no. 7, pp. 442–444, Jul. 2015.
[17] J. Valencia, V. E. Boria, M. Guglielmi, and S. Cogollos, "Compact wideband hybrid filters in rectangular waveguide with enhanced out-of-band response," *IEEE Trans. Microw. Theory Techn.*, vol. 68, no. 1, pp. 87–101, Jan. 2020.
[18] P. Booth and E. V. Lluch, "Enhancing the performance of waveguide filters using additive manufacturing," *Proc. IEEE*, vol. 105, no. 4, pp. 613–619, Apr. 2017.
[19] P. Vallerotonda, L. Pelliccia, C. Tomassoni, F. Cacciamani, R. Sorrentino, J. Galdeano, and C. Ernst, "Compact waveguide bandpass filters for broadband space applications in C and Ku-bands," in *Proc. Eur. Microw. Conf. Central Eur. (EuMCE)*, 2019, pp. 116–119.
[20] R. V. Snyder and S. Bastioli, "Broad passband, wide stopband, high power evanescent mode filters using capacitively-loaded ridges," in *Proc. 42nd Eur. Microw. Conf. (EuMC)*, Oct. 2012, pp. 176–179.
[21] X. Shang, P. Penchev, C. Guo, M. J. Lancaster, S. Dimov, Y. Dong, M. Favre, M. Billod, and E. de Rijk, "*W*-band waveguide filters fabricated by laser micromachining and 3-D printing," *IEEE Trans. Microw. Theory Techn.*, vol. 64, no. 8, pp. 2572–2580, Aug. 2016.
[22] J. Li, C. Guo, L. Mao, J. Xiang, G.-L. Huang, and T. Yuan, "Monolithically 3-D printed hemispherical resonator waveguide filters with improved out-of-band rejections," *IEEE Access*, vol. 6, pp. 57030–57048, 2018.
[23] Renishaw Plc. *RenAM 500Q*. Accessed: Jan. 21, 2022. [Online]. Available: https://www.renishaw.com/en/renam-500q–42781
[24] C. Silbernagel, I. Ashcroft, P. Dickens, and M. Galea, "Electrical resistivity of additively manufactured AlSi10Mg for use in electric motors," *Additive Manuf.*, vol. 21, pp. 395–403, May 2018.
[25] K. Kempen, L. Thijs, J. Van Humbeeck, and J.-P. Kruth, "Mechanical properties of AlSi10Mg produced by selective laser melting," *Phys. Proc.*, vol. 39, pp. 439–446, Jan. 2012.

POVILAS VAITUKAITIS (Graduate Student Member, IEEE) received the M.Eng. degree (Hons.) in mechanical engineering from the University of Aberdeen, Aberdeen, U.K., in 2019. He is currently pursuing the Ph.D. degree in electrical engineering with Heriot-Watt University, Edinburgh, U.K.

His current research interests include microwave passive device design and manufacturing using metal additive manufacturing technologies.

Prof. Vaitukaitis received the Project Award for an outstanding master's thesis project from the Institution of Mechanical Engineers (IMechE), in 2019.

KENNETH NAI received the B.Sc. degree (Hons.) in electronics and electrical engineering and the Ph.D. degree in control systems from Loughborough University, Loughborough, U.K., in 1990 and 1995, respectively.

He has been in employment with Renishaw PLC, Wotton-Under-Edge, U.K., since 1995, where he is currently a Principal Engineer and has developed products in the field of metrology systems, neurosurgical robotics, and metal powder 3-D printers. He has been granted 11 U.S. patents.

Dr. Nai is also a Chartered Engineer and a member of the Institution of Engineering and Technology.

JIAYU RAO (Graduate Student Member, IEEE) received the M.Sc. degree (Hons.) in electronics science and technology from the China University of Mining and Technology (CUMT), Xuzhou, China, in 2018. He is currently pursuing the Ph.D. degree with the School of Engineering and Physical Sciences, Heriot-Watt University (HWU), Edinburgh, U.K.

His research interests include radio frequency (RF)/microwave passive device's miniaturization and integration, such as high-Q filters, filter/antennas, and filter/antenna arrays using 3-D metal printing and substrate integrated waveguide (SIW) technologies.

JIASHENG HONG (Fellow, IEEE) received the D.Phil. degree in engineering science from the University of Oxford, Oxford, U.K., in 1994.

Then, he joined the University of Birmingham, Birmingham, U.K., until 2001, when he moved up to Edinburgh, U.K., to join Heriot-Watt University, Edinburgh, where he is currently a Professor leading a team for research into advanced radio frequency (RF)/microwave device technologies. He has authored or coauthored over 200 journal articles and conference papers in this field and has published four relevant books: *Microstrip Filters for RF/Microwave Applications* (Wiley, first edition, 2001, and second edition, 2011), *RF and Microwave Coupled-Line Circuits* (Artech House, second edition, 2007), *Balanced Microwave Filters* (Wiley, 2018), and *Advances in Planar Filters Design* (IET, 2019).

Dr. Hong is also a member of the IEEE MTT Technical Committees, a Subject Editor of *Electronics Letters* (Microwave), and an Associate Editor of *IET Microwaves, Antennas & Propagation* and *International Journal of RF and Microwave Computer-Aided Engineering*.